

Characterization of Adhesive Microstructures for Improved Bonding in Embedded Sensors

Nicholas C. Reed¹, Rishikesh Srinivasaraghavan Govindarajan², and Daewon Kim³

Embry-Riddle Aeronautical University, Daytona Beach, Florida, 32114, United States

Creating efficient sensing technologies and successfully integrating them into real-world applications poses unique challenges. One of the major challenges is integrating sensing elements into a desirable substrate. Additive manufacturing (AM) has emerged as a promising technique for improving this integration. To enhance the structural performance of embedded sensors, adhesive microstructures are added during the manufacturing process. These microstructures increase surface area, leading to stronger bonds and improved performance. However, maximizing surface area may not always be suitable for small sensors, requiring improvement of microstructure design within certain limits. Peel tests were conducted using AM test arrays to assess the ideal ranges of microstructures. Results showed that increasing surface area enhances adhesive force, but the relationship is nonlinear. The sizing of microstructures, particularly aspect ratio and spacing, significantly affects adhesive force, with optimal performance observed at specific aspect ratios and spacings. The sensor with the optimal microstructure was tensile tested and determined to increase the adhesive performance without any detrimental mechanical impact.

I. Nomenclature

AM = Additive Manufacturing

A.U. = Arbitrary Units

CZM = Cohesive Zone Model
DIC = Digital Image Correlation
IPA = Isopropyl Alcohol

LCD = Liquid Crystal Display

UV = Ultraviolet

II. Introduction

Developing effective sensing technologies and integrating them into practical applications is a complex process. One of the largest challenges in embedded technologies involves the integration of the sensing elements into a desirable substrate. Additive manufacturing (AM) is one of the primary emergent techniques to improve this integration process, due to its ability to produce unique structures efficiently and rapidly [1-6]. Sensors can be included into a partially-complete matrix, which is then finished into a completed package. However, the specifics and practicality of this integration is more complicated than typical solid structures. The act of integrating a sensor into a part creates new structural issues, such as debonding and substrate weakness typically seen in composite laminate failure [3, 4, 6, 7]. As such, the expected performance response of structures with embedded parts is often overlooked, and improving these characteristics structurally needs additional support.

¹ Graduate Student, Department of Aerospace Engineering, AIAA Student Member

² Graduate Student, Department of Aerospace Engineering

³ Professor, Department of Aerospace Engineering, AIAA Senior Member.

One of the primary developing techniques used to improve sensor structural performance involves adding performance-enhancing adhesive microstructures to the sensor or substrate during the manufacturing process [3]. This technique is commonly found frequently in nature, at a large variety of scales [2, 8-11]. By adding these structures, the peak loading conditions and overall operation lifetime can be improved, and if AM processes are used in the fabrication of the sensor and substrate, these specific quantities can be tuned. This can enable the use of otherwise unsuitable materials in an embedded sensing scenario.

The main functionality that adhesive microstructures provide is an increase of the surface area, improving the area of contact for adhesive forces to act upon, which is well known to produce a stronger bond. As such, improving the sensor's microstructure can enhance overall performance. However, in certain applications, maximizing surface area may not always be the best approach, such as with very small sensors where microstructures have certain size restrictions [2, 11, 12]. In these situations, the focus shifts from maximizing surface area to augmenting the design of the microstructure for maximum efficiency within certain limits. By designing microstructures that are specifically tailored to the size of the sensor and substrate, the embedded part can be improved without compromising on design changes. By utilizing the flexibility of an AM fabrication approach, new designs can be rapidly manufactured, tested for performance, and applied to practical sensing solutions to increase the sensor lifetime.

III. Experimental Design

This section describes the design of the structure tests, the parameters studied, and the validation of the embedded design in mechanical testing.

A. Experimental Procedures

To test the ideal ranges for microstructures, a series of modified ASRM D903 peel tests were performed on various pillar microstructures. The structures were printed with a standard high resolution acrylate photocurable resin on a Phrozen Sonic Mini8k Liquid Crystal Display (LCD) printer. The samples were modified from the standard via scaling down to fit within the printable area of the LCD printer, dimensions as shown in Fig. 1. After printing, a layer of Sylgard 186, a type of polydimethylsiloxane (PDMS), was applied to the test coupon. These structures were treated with a post-processing technique to enable complete curing of the PDMS without any "poisoning" effects typical of photocurable resins with PDMS [5]. First, the printed and cured parts are baked at 120 °C for 8 hours. After being allowed to cool, they are rinsed in isopropyl alcohol (IPA) and air dried for 30 minutes. Then, the samples are treated with a 400-watt ultraviolet (UV) lamp for 120 seconds. They are fully rinsed again, and allowed to air dry. This bake and UV cycle is performed for a second time. Finally, immediately before application of PDMS, the samples are cured with oxygen plasma for 20 seconds. The oxygen plasma was configured with a chamber pressure of 149.9 mmHg, 25 W power, and a flow rate of 20 cc/min. After production, the samples were configured within an Amatek CS225 Chatillon load frame fitted with a 10 lb. load cell, and pulled at a rate of 305 mm/min. The loading response was recorded and the average stabilized load per unit width was recorded.

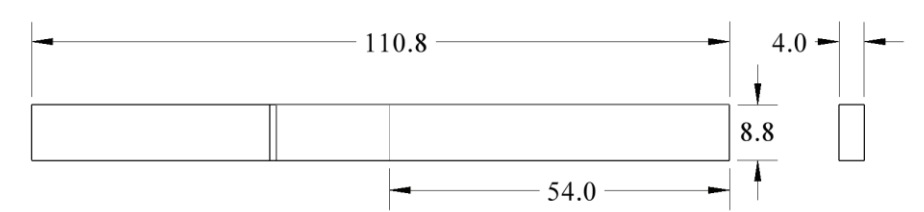


Fig. 1 Modified D903 Sample Dimensions, in mm. This sample pattern is utilized in peel testing.

B. Parameter Design

A series of several parameters regarding the pillar structure were investigated. The main characteristics of a structure that can be modified are the sizing, the aspect ratio, and the spacing. By altering these, all other dimensions of the structure are controlled for. These parameters, in turn, determine the effective surface area and volume of the total structures, as well as control the amount of deformation required to fully detach the two layers. Three tests were devised to explore varying the sizing, aspect ratio, and spacing of the microstructure. The key parameters were varied over a range, and the loading responses were recorded. From the loading response, the average stabilized load per unit width was recorded. To track the effects of mechanical interference in the efficiency of the microstructures, the data was also normalized with respect to surface area, to eliminate the effect of larger surface area on adhesion. Initially,

the structures have even height, width, and spacing. After identifying the most efficient parameter, it was used in future test samples as a fixed value. An example of a successfully printed microstructure pattern is shown in Fig. 2.

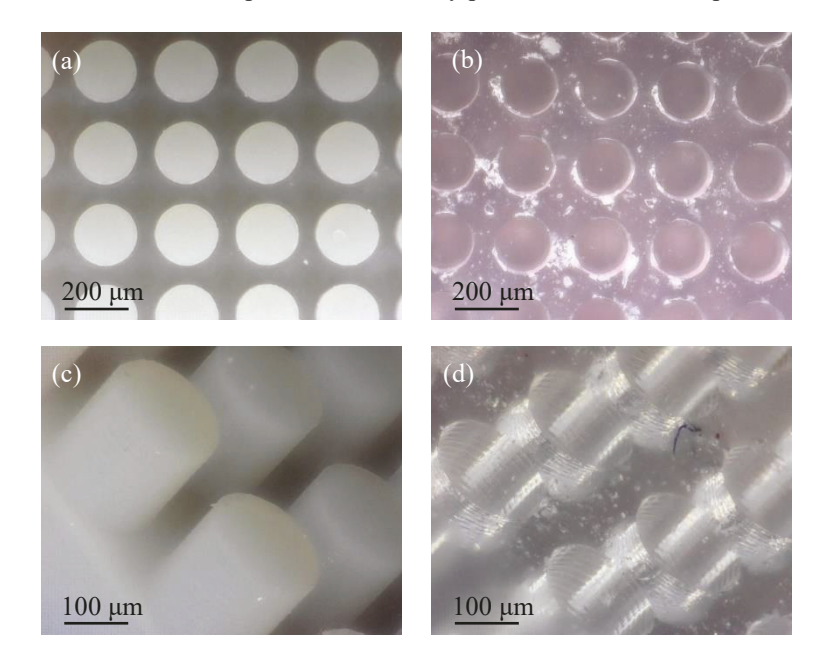


Fig. 2 (a) An example of the printed pillar structure (200 μm height x 200 μm diameter) after testing debonding. Note the clean patterning, with no visible residue on the master mold. (b) The demolded Sylgard 186 inverse pattern. Note the clean impression (aside from debonded polymer debris), with no loss of detail. (c) A close-up image of the printed pillar structures. (d) A close-up of the demolded Sylgard 186 inverse pattern. The individual layers (~10 μm height) are distinct and visible, indicating no "poisoning" effect occurred.

C. Embedded Sensor Adhesion Validation

After determining the optimal parameters for the adhesive microstructure, an embedded tensile test is performed. Utilizing the extant LCD vat polymerization process, the structure-enhanced sensor is fabricated and integrated into a flexible tensile coupon to be tested. A dogbone test structure is modified from ASTM D638, as shown in Fig. 3, similarly scaled down to fit within the printable area of the LCD printer. Inside the dogbone, a small sensor cavity is present, which allows the structured sensor to be inserted during the printing process. After the sensor is inserted, uncured flexible photopolymer resin is allowed to flow into the cavity, removing the open space surrounding the sensor and filling in the microstructure. The dogbone coupon is then allowed to fully print, and is flood cured after the removal of excess liquid resin. This solidifies the internal cavity, completely sealing the sensor inside the dogbone and fusing the remaining resin, removing the cavity and completely encasing the sensor. Before the dogbones are brought to failure, they are scanned with a Bruker SkyScan X-ray microtomography machine, to provide high-resolution scans of the sensor and ensure the embedded dogbone is free of manufacturing defects.

After the embedded coupon is produced and post-processed, it is treated with a paint speckle pattern for analysis utilizing Digital Image Correlation (DIC). Utilizing VIC-3D, a fully featured DIC software suite, the strain field response of the sensor can be tracked during a tensile test, and the overall sensor health can be monitored, including when delamination or sensor damage occurs. An MTS Criterion 310 is used to pull the dogbones until failure at a constant rate of 5 mm/min, during which DIC images are taken. After the dogbones are brought to failure, they are scanned again with X-ray microtomography to identify any internal damage.

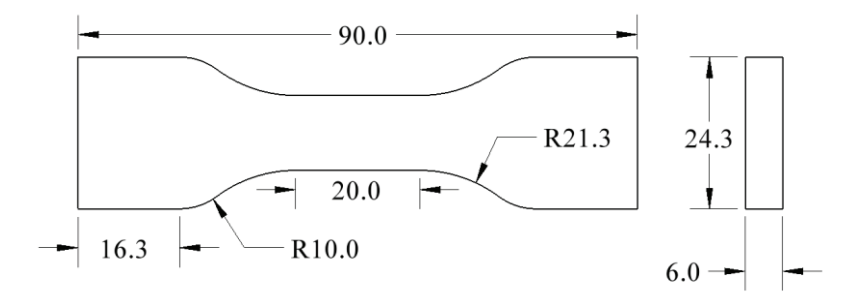


Fig. 3 Modified D638 Sample Dimensions, in mm. This sample pattern is utilized in tensile testing.

IV. Results

A. Peel Test Parameter Selection

The results showed that, while increasing the surface area universally increases adhesive force, the increase is not perfectly linear, and begins to slow after a certain amount of variation. Fig. 4 shows the results of the sizing tests, both raw and normalized. Notably, when the sizing of the microstructure is with respect to spacing and aspect ratio, the total surface area of the microstructure does not significantly change. Because of this, there are only slight variations in the adhesion values for the larger structure. With the minor variations in the surface area normalized, it can be observed that the mechanical adhesion effects are minimal for sizing, allowing the specific optimal sizing to be determined for aspect ratio, spacing, and overall application scale.

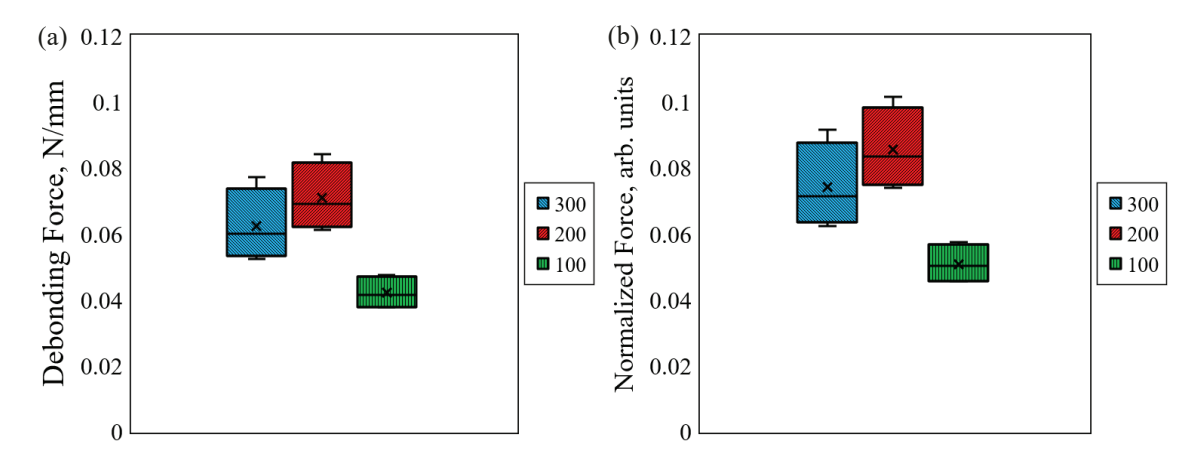


Fig. 4 Results for the variable sizing test: (a) raw force per unit length and (b) normalized force per unit length. The numbers in legend correspond to a structure's height, diameter, and spacing simultaneously, in μm. The 200 μm microstructure showed the best performance. The normalization diminutively alters the data, as the total surface areas between the three cases are largely the same.

Fig. 5 shows the results of the aspect ratio test. The aspect ratio shows a large increase around 2 diameter heights (400 μ m), with a less dramatic increase at 4 diameter heights, and several drops in efficacy at and below 1 diameter height. Normalized with respect to surface area, this corresponds to a high efficiency at an aspect ratio of 2, with less adhesion being gained from increasing the height of the structures, and significantly worse performance with an aspect ratio of less than 1.

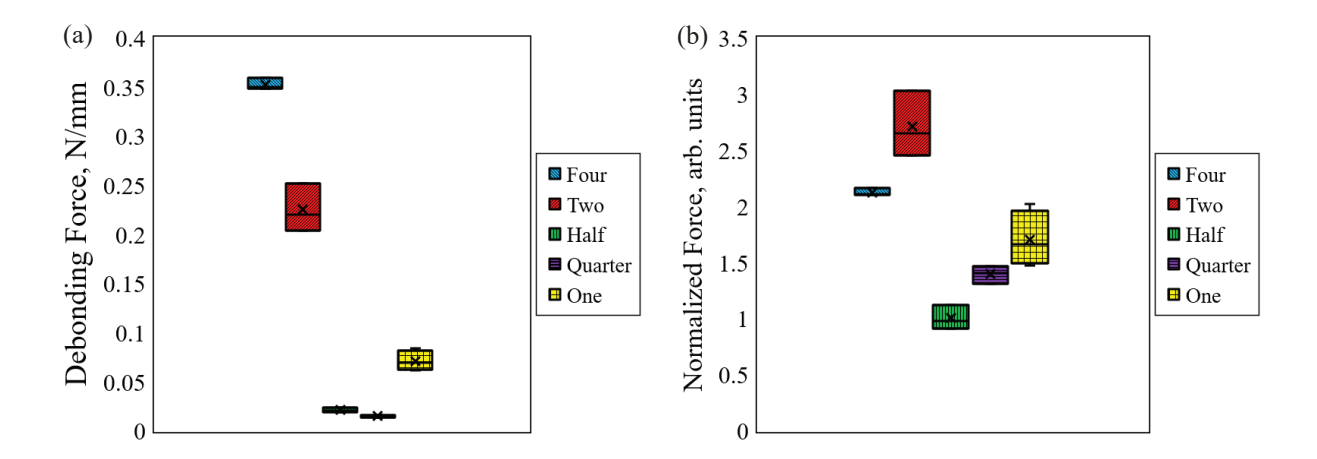


Fig. 5 Result for the variable aspect ratio test: (a) raw force per unit length and (b) normalized force per unit length. The 4 AR structure showed the overall best performance, with the 0.25 AR performing the worst. When normalized for increased surface area; however, the 2 AR structures have significantly better performance, indicating a stronger mechanical interference.

Fig. 6 shows the results of the spacing test. The spacing shows a large increase above 1 diameter spacing, with the best results peaking around $\frac{1}{2}$ diameter (100 μ m), and several drops in efficacy above 1 diameter spacing. Normalized with respect to surface area, this corresponds to a higher relative efficiency at a $\frac{1}{2}$ diameter spacing, with adhesion dropping when both increasing and decreasing the spacing.

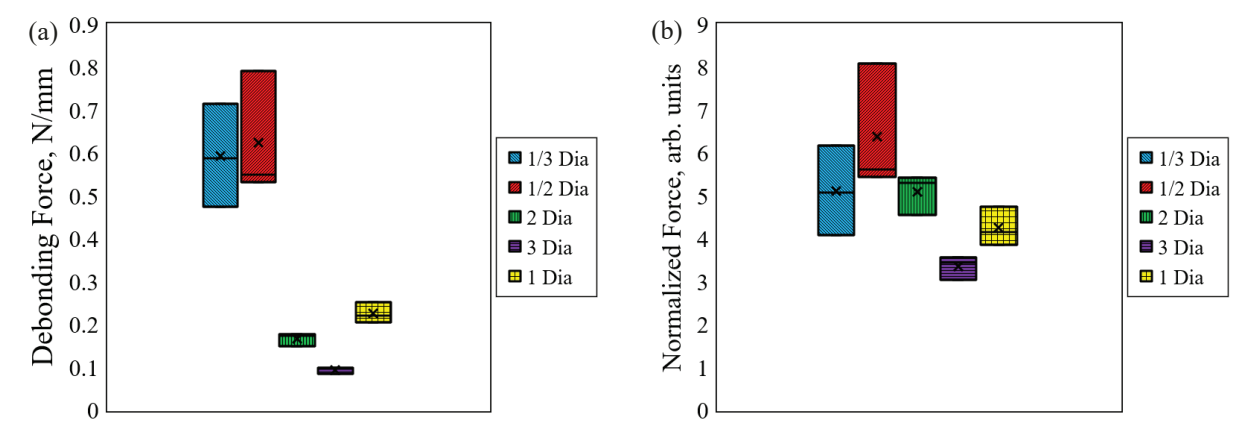


Fig. 6 Result for the variable spacing test: (a) raw force per unit length and (b) normalized force per unit length. The ½ diameter spacing showed the overall best performance, with the 3 diameter spacing performing the worst. When normalized for increased surface area, the ½ diameter spacing still performs better.

B. Optimal Microstructure Cohesive Zone Model

In the pursuit of a more in-depth examination of the tangible benefits provided by the adhesive microstructure and the enhancement of its properties, a numerical model was developed for the optimal adhesive microstructure (200 µm diameter, 400 µm height, 100 µm spacing). To accomplish this task, a Cohesive Zone Model (CZM) has been incorporated into an ANSYS Mechanical simulation that emulates the debonding process of sensor materials from the substrate material. To illustrate the model, a simple plate delamination was simulated. When exposed to a uniform vertical deformation, the plate structure without the simulated microstructure experiences significantly more delamination along the bond line, and experiences a significantly smaller loading force required for the deformation.

The developed CZM model was then used to simulate a Mode I failure in an embedded sensor system. A thin, stiff plate, representing a typical sensor, is encased in a larger substrate, here modeled as PDMS. The embedded system is then loaded on the exterior of the substrate, emulating the conditions of a developing Mode I fracture. Fig. 7(a and b) demonstrates the simulated fracture response for a sensor with and without microstructure. After the loading is fully applied, the sensor without simulated structure begins to delaminate, indicating a premature sensor failure due to delamination. However, the sensor with simulated structure does not begin to delaminate, instead causing more significantly substrate deformation. Fig. 7(c) plots the gap in the contact region for the two simulated Mode I fracture loading phases. It is clear that the structure prevents the rapid gap increase at the bond interface.

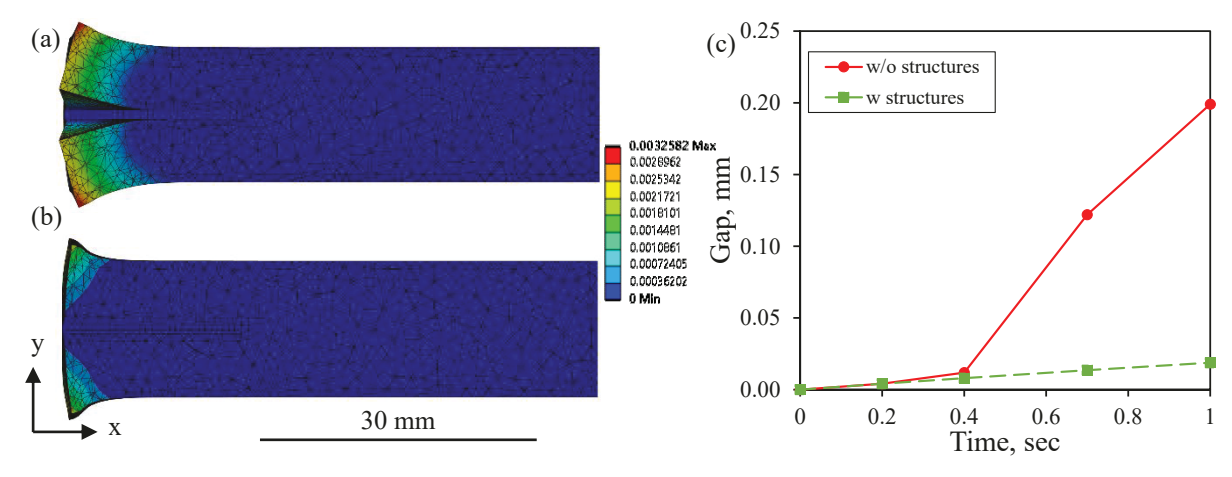


Fig. 7 Cutaway of microstructure CZM simulation for Mode I fracture at 15 N. (a) The unstructured sample shows significant signs of fracture at the interface between the sensor and substrate, while (b) the structured sample only shows localized deformation, with no evidence of fracture, indicating a clean bond between the sensor and substrate. (c) The exact contact displacement graph shows the large crack only present in the sensor without adhesive structures.

C. Embedded Sensor Testing and Validation

The results of the embedded coupon tests are shown below. The dogbone tests universally showed both an increase in sensor longevity without any reduction in sensing capabilities, and significantly increased bonding performance in the structured regions.

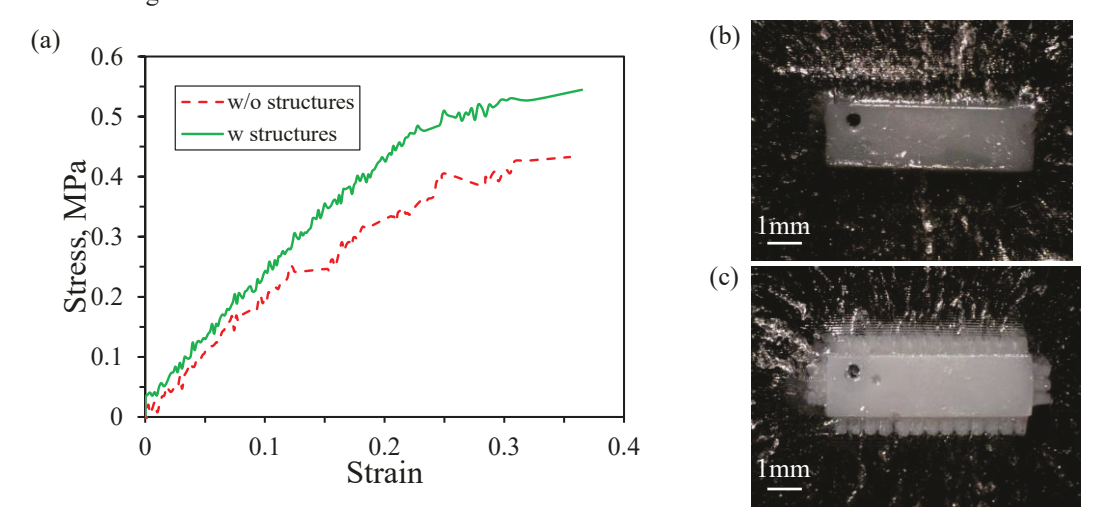


Fig. 8 Results for the flexible embedded sensor dogbones. (a) Stress-Strain curves of these dogbones indicate similar mechanical performance with the embedded sensor, regardless of structure. Post failure, microscopy of (b) the smooth embedded sensor shows emergent cracks on the exposed edges of the smooth sensor. (c) The structured sensor instead shows intact bonding around the exposed edges.

The flexible dogbone tests showed similar deflections for both structured and unstructured sensors, as shown in Fig. 8(a). Both cases failed at the unstructured boundary, which caused internal cracking that failed the structure. DIC strain maps of the samples before failure demonstrate a region of decreased strain directly underneath a region of increasing strain. The relatively stiffer region represents the sensor, and the strain concentration correlates to the delamination and internal cracking. Microscopy of the failed samples indicates clear weakness around the unstructured regions of the embedded sensors, even in places where the sample had not fully delaminated from the substrate, as shown in Fig. 8(b). In contrast, the structured regions on the embedded sensor remain fully embedded, showing no signs of debonding, as seen in Fig. 8(c). Notably, there was no visible delamination or damage before the deformation as captured by X-ray microtomography.

Fig. 9(a) shows similar loading curves of stiff dogbone tests for both the structured and unstructured dogbones mirroring the results of the flexible dogbone tests. These samples, too, failed from internal cracking, with a stress concentration located above a stiffer region surrounding the sample. The structure appears to have a minor beneficial effect on the dogbones strength, likely due to the reduction in potential crack initiation sites with the well-bonded structured surfaces. The embedded sensor's resistance responses for both dogbones shows good linearity, but varies in terms of overall lifespan, as shown in Fig. 9(b). The unstructured sensor suffered from an early failure with the wiring becoming sheared from the sensor; a crack had formed on one of the edges that was delaminating. This shearing, however, did not occur on the structured sensor, which likely did not have the same delamination at the early stages of deflection. The structured sensor shows irregularity around the 0.06 to 0.08 mm/mm strain region, where the sample physically warped before mechanically failing.

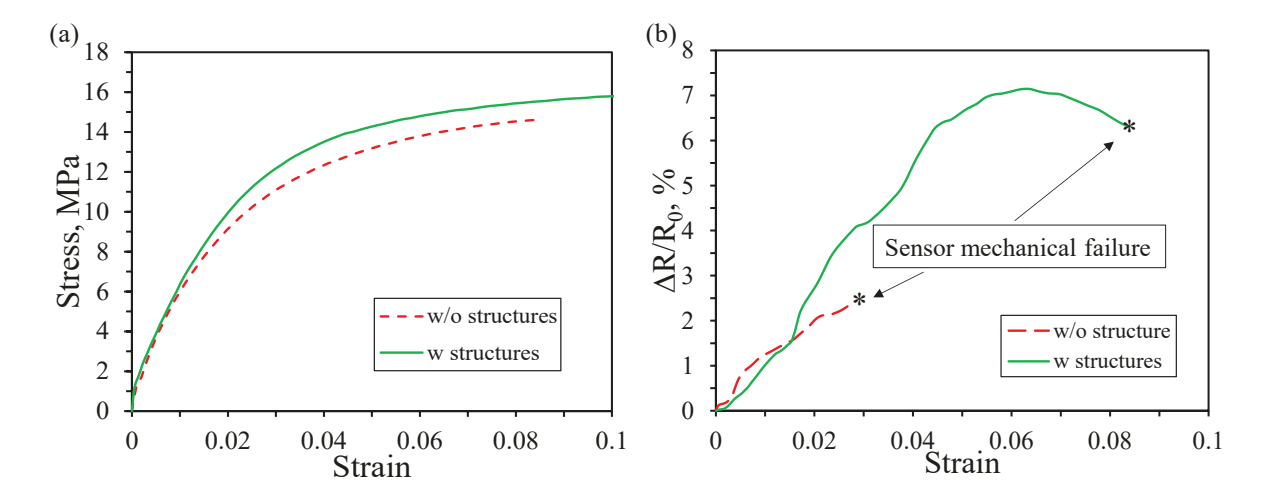


Fig. 9 Results for the stiff embedded sensor dogbones. (a) Stress-Strain curves of these dogbones indicate similar mechanical performance with the embedded sensor, regardless of structure. (b) Resistance-Strain curves indicate good linearity, and demonstrate the increased performance of the microstructured sample.

The structured sensor endures significantly more deformation before failing.

V. Conclusion

In this work, we explore the development and implementation of adhesive microstructure designed to improve the functionality of embedded sensing technologies. With an optimal structure parameter set analyzed and tested, future work includes the development of an analytical and computational model of these structures, as well as further investigation into the selection of shape design to greatly increase adhesive performance. The emphasis on AM techniques as a driving force increases both the flexibility and the scalability of the proposed techniques. Therefore, the advancement of integrated functional microstructure holds promise for customizable enhancement of AM sensor systems in future applications. The increase in adhesive performance offers little downside and has the potential to produce tailored solutions to difficult sensing integration challenges.

Acknowledgments

This material is based upon work supported by the National Science Foundation under Grant No. 2229155. The opinions, findings, and conclusions, or recommendations expressed are those of the authors and do not necessarily reflect the views of the National Science Foundation.

References

- [1] Sikulskyi, S., Ren, Z., Mekonnen, D. T., Holyoak, A., Srinivasaraghavan Govindarajan, R., and Kim, D., "Additively Manufactured Unimorph Dielectric Elastomer Actuators: Design, Materials, and Fabrication," Frontiers in Robotics and AI, Vol. 9, 2022, p. 1034914. https://doi.org/10.3389/frobt.2022.1034914
- [2] Huang, T. Q., Qu, X., Liu, J., and Chen, S., "3D Printing of Biomimetic Microstructures for Cancer Cell Migration," Biomedical Microdevices, Vol. 16, No. 1, 2014, pp. 127–132. https://doi.org/10.1007/s10544-013-9812-6
- [3] Arzt, E., Quan, H., McMeeking, R. M., and Hensel, R., "Functional Surface Microstructures Inspired by Nature From Adhesion and Wetting Principles to Sustainable New Devices," Progress in Materials Science, Vol. 120, 2021, p. 100823. https://doi.org/10.1016/j.pmatsci.2021.100823
- [4] Pang, C., Zhao, Z., Du, L., and Fang, Z., "Adhesive Bonding with SU-8 in a Vacuum for Capacitive Pressure Sensors," Sensors and Actuators A: Physical, Vol. 147, No. 2, 2008, pp. 672–676. https://doi.org/10.1016/j.sna.2008.06.001
- [5] Venzac, B., Deng, S., Mahmoud, Z., Lenferink, A., Costa, A., Bray, F., Otto, C., Rolando, C., and Le Gac, S., "PDMS Curing Inhibition on 3D-Printed Molds: Why? Also, How to Avoid It?," Analytical Chemistry, Vol. 93, No. 19, 2021, pp. 7180– 7187. https://doi.org/10.1021/acs.analchem.0c04944
- [6] Wandowski, T., Moll, J., Malinowski, P., Opoka, S., and Ostachowicz, W., "Assessment of Piezoelectric Sensor Adhesive Bonding," Journal of Physics: Conference Series, Vol. 628, 2015, p. 012114. https://doi.org/10.1088/1742-6596/628/1/012114
- [7] Mayuet, P. F., Girot, F., Lamíkiz, A., Fernández-Vidal, S. R., Salguero, J., and Marcos, M., "SOM/SEM Based Characterization of Internal Delaminations of CFRP Samples Machined by AWJM," Procedia Engineering, Vol. 132, 2015, pp. 693–700. https://doi.org/10.1016/j.proeng.2015.12.549
- [8] George, R. P., Muraleedharan, P., Sreekumari, K. R., and Khatak, H. S., "Influence of Surface Characteristics and Microstructure on Adhesion of Bacterial Cells onto a Type 304 Stainless Steel," Biofouling, Vol. 19, No. 1, 2003, pp. 1–8. https://doi.org/10.1080/08927010290031017
- [9] Gorb, E., and Gorb, S., "Contact Separation Force of the Fruit Burrs in Four Plant Species Adapted to Dispersal by Mechanical Interlocking," Plant Physiology and Biochemistry, Vol. 40, No. 4, 2002, pp. 373–381. https://doi.org/10.1016/S0981-9428(02)01381-5
- [10] Nadler, J. H., Mercer, A. J., Culler, M., Ledford, K. A., Bloomquist, R., and Lin, A., "Structures and Function of Remora Adhesion," MRS Proceedings, Vol. 1498, 2013, pp. 159–168. https://doi.org/10.1557/opl.2013.105
- [11] Zhou, Y., Xiao, Y., Qiu, Y., Yuan, H., Van Blitterswijk, C. A., Zhou, X., Xu, X., and Bao, C., "Adhesion and Proliferation of Cells and Bacteria on Microchip with Different Surfaces Microstructures," Biomedical Engineering / Biomedizinische Technik, Vol. 61, No. 5, 2016. https://doi.org/10.1515/bmt-2015-0075
- [12] Chen, Y.-C., and Yang, H., "Octopus-Inspired Assembly of Nanosucker Arrays for Dry/Wet Adhesion," ACS Nano, Vol. 11, No. 6, 2017, pp. 5332–5338. https://doi.org/10.1021/acsnano.7b00809